

Noninvasive Imaging of Melanoma with Reflectance Mode Confocal Scanning Laser Microscopy in a Murine Model

Daniel S. Gareau^{1,2}, Glenn Merlino³, Christopher Corless^{1,2}, Molly Kulesz-Martin^{1,2} and Steven L. Jacques^{1,2}

A reflectance-mode confocal scanning laser microscope (rCSLM) was developed for imaging early-stage melanoma in a living mouse model without the addition of exogenous contrast agents. Lesions were first located by surveying the dorsum with a polarized light camera, then imaged with the rCSLM. The images demonstrated two characteristics of melanoma in this animal model: (1) melanocytes and apparent tumor nests in the epidermis at the stratum spinosum in a state of pagetoid spread and (2) architectural disruption of the dermal-epidermal junction. The epidermal melanocytes and apparent tumor nests had a high melanin content, which caused their reflectance to be fivefold greater than the surrounding epidermis. The rCSLM images illustrate the difference between normal skin and sites with apparent melanoma. This imaging modality shows promise to track the progression of melanoma lesions in animal models.

Journal of Investigative Dermatology (2007) **127**, 2184–2190; doi:10.1038/sj.jid.5700829; published online 26 April 2007

INTRODUCTION

Reflectance-mode confocal microscopy (rCSLM) offers a means to image mouse skin *in vivo* by exploiting scattering from microscopic biological variations in refractive index. The light-scattering properties of cutaneous tissues provide optical contrast for imaging the presence and spatial distribution of pigmented melanoma against the background of healthy tissue in a pigmented murine model, the hepatocyte growth factor/scatter factor transgenic mouse (HGF/B6) (Noonan *et al.*, 2001). Components of skin whose refractive index are higher than the bulk refractive index of epidermis ($n_{\text{epi}} = 1.34$) (Rajadhyaksha *et al.*, 1999), such as keratin in stratum corneum ($n = 1.51$) (Rajadhyaksha *et al.*, 1999), hydrated collagen ($n = 1.43$) (Wang *et al.*, 1996), and melanin ($n = 1.7$) (Vitkin *et al.*, 1994) can be imaged with backscattered light.

Conventional wide-field microscopy illuminates and images a large volume simultaneously, so thin histological sections must be prepared to observe structural, cellular, and subcellular details. Optical sectioning in rCSLM blocks multiply scattered light so the image of the tissue in the

plane of focus remains sharp despite light scattered above and below that plane. Confocal microscopy is limited in depth to the ballistic regime where photons propagate unscattered to the focus, backscatter from the focus toward the microscope, and escape the tissue without scattering. At deeper depths, the low level of light owing to multiply scattered photons becomes the optical noise floor for the image, specifying the practical depth limit for rCSLM imaging. The imaging depth range of rCSLM in this work (50–100 μm) was limited primarily by the laser wavelength used (488 nm). As mouse epidermis is thin ($\sim 15 \mu\text{m}$, Figure 3), even enlarged epidermis ($\sim 40 \mu\text{m}$, Figure 4b) associated with tumors can be imaged fully. By comparison, imaging with rCSLM in human skin (Rajadhyaksha *et al.*, 1999) with 830-nm laser light encounters 1.7-fold less scattering and 4 fold less optical absorption (Jacques, 1998). The imaging depth is increased to 250 μm , which sufficiently images human epidermis (60–100 μm).

The long-term goal of this work is to contribute to ongoing efforts to “humanize” the mouse melanoma model such that melanoma onset in the mouse model better mimics early stage human melanoma where tumors originate in the interfollicular epidermis and invade locally downward through the epidermal-dermal junction (DEJ) rather than originating in the deeper dermis as in current mouse models. In human skin, melanomas are characterized by polymorphic (multilobed) melanocytes (Greger *et al.*, 2005). One goal of this work was to survey the features of this animal model and identify characteristic structures that occur only in melanoma and not in normal skin (Figure 7).

The rCSLM images can detect the early progression of melanoma in the subepidermal layer and its violation of the

¹Department of Dermatology, Oregon Health & Science University, Portland, Oregon, USA; ²Department of Biomedical Engineering, Oregon Health & Science University, Portland, Oregon, USA and ³Laboratory of Cell Regulation and Carcinogenesis, National Cancer Institute, Bethesda, Maryland, USA

Correspondence: Dr Daniel S. Gareau, Department of Dermatology, Memorial Sloan Kettering Cancer Center, Dermatology, 160 E. 66th, New York, New York 10022, USA. E-mail: dan@dangareau.net

Abbreviations: DEJ, epidermal-dermal junction; HGF, hepatocyte growth factor; rCSLM, reflectance-mode confocal scanning laser microscope

Received 22 August 2006; revised 30 January 2007; accepted 9 February 2007; published online 26 April 2007

DEJ by revealing melanocytic structures in this well-characterized animal model of UV-induced melanoma (Noonan *et al.*, 2001). Melanoma can be characterized by the high reflectance from melanocytes and strong attenuation within tumors. Melanin granules (~30 nm diameter within melanosomes) have a refractive index of 1.7 (Vitkin *et al.*, 1994) compared with the surrounding cytoplasm of 1.35 (Brunsting and Mullaney, 1974). Therefore, melanin granules scatter light, providing a strong endogenous contrast agent for rCSLM (Rajadhyaksha *et al.*, 1995) image of melanocytes. The two key features of melanoma imaged by rCSLM were (1) pagetoid melanocytes and tumor nests in the epidermis and (2) altered skin ultrastructure described as the disruption of the DEJ. The ability of rCSLM to image the development of these features suggests that time course imaging may elucidate the dynamically invasive nature of melanoma lesions in this mouse model.

RESULTS

Excised samples were fixed in formalin, sectioned, and stained using hematoxylin and eosin. Samples stained with a histological counter stain for iron pigment showed that the pigment was in fact melanin. A melanin-bleach method revealed subcellular detail in melanoma cells verifying the atypical nuclei in tumor cells. Immunohistochemical staining with the antibody PEP8H specified the melanocyte antigen dopachrome tautomerase (DCT) and verified the presence of melanocytes. Figure 1 shows an immunohistochemically stained tumor biopsy.

Figure 2a and b shows a typical experiment where a lesion is identified and imaged over 3 weeks. The nodular tumor is indicated both with and without involvement of the surrounding dermis. This rapid nodular growth developed in approximately half of the observed tumors.

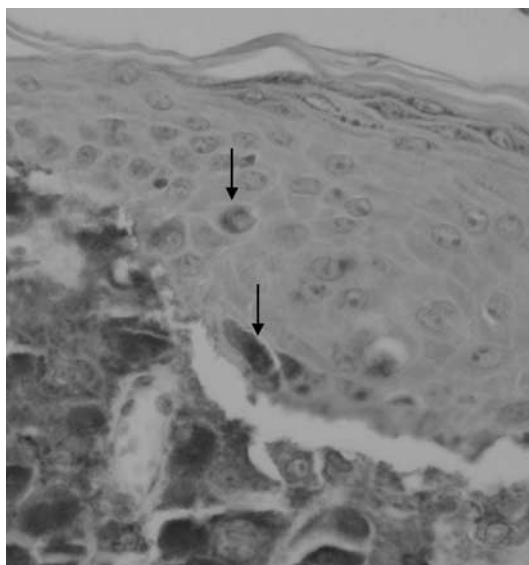


Figure 1. The immunohistochemical stain for dopachrome tautomerase verifies that the tumor is a melanoma. Epidermal melanocytes are shown with arrows.

Eight lesions identified by polarized imaging showed suspicious areas of uneven confocal reflectance in the epidermis and at the DEJ. Five normal sites (Figure 3) were characterized in a sagittal view (image of a plane perpendicular to the surface) by a relatively uniform reflectance with the absence of highly reflective structures. As a measure of

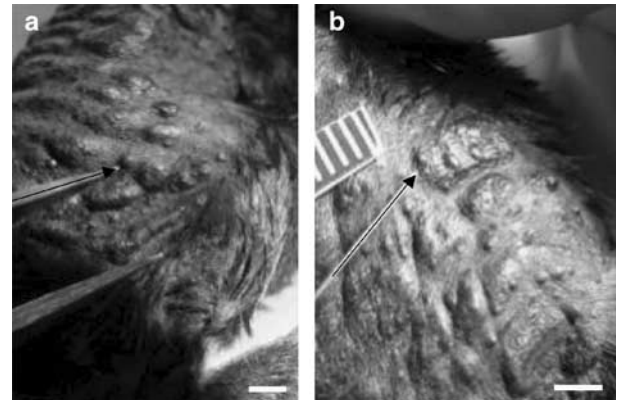


Figure 2. Digital photography of tumors. Digital photograph of (a) early-stage tumor and (b) late-stage tumor 2 weeks later. Bar = 4 mm.

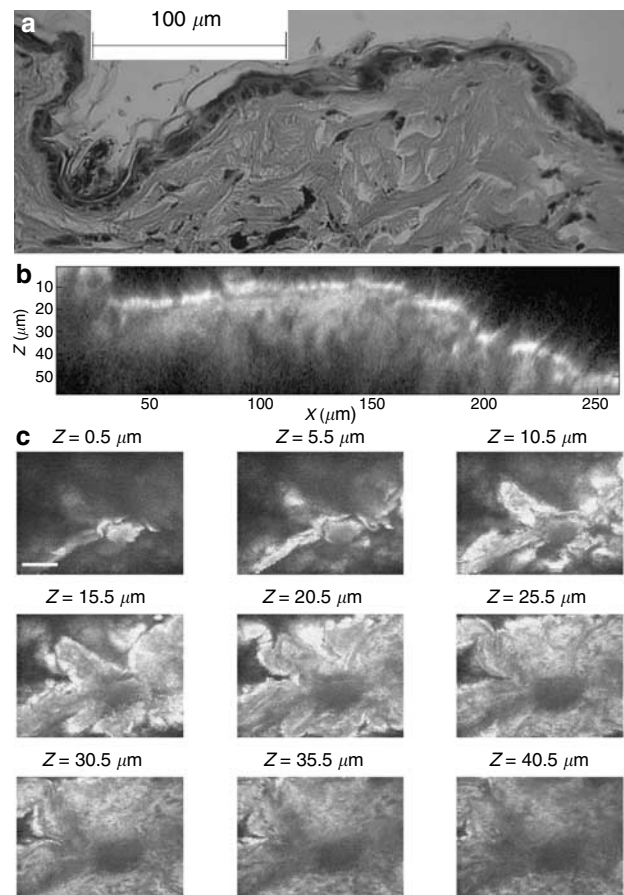


Figure 3. Normal skin. Figure of normal skin, correlating histology (a) with confocal microscopy of normal skin in (b) sagittal view. (c) A set of *en face* images taken at various depths on a different normal skin site.

dermal reflectance uniformity, the maximum contrast (brightest voxel value divided by dimmest) was 1.3 ± 0.2 . Normal epidermis was about $15 \mu\text{m}$ thick (one or two cell layers) based on the histological image (Figure 3a). Collagen reflectance in the underlying dermis was uniform and the DEJ was relatively flat. Melanocytes were sparse among

keratinocytes, yet frequent enough to give the skin a dark tone to the eye. Melanocytes accounted for less than 1% of epidermal cells as observed by rCSLM and histology. In contrast, melanoma lesions were well populated with pleomorphic melanocytes and melanocyte nests.

Melanoma lesions contained high levels of melanin and were located repeatedly as dark regions in wide-field images and bright regions in subepidermal microscopic images. Malignant tumors presented nodular regions of high reflectance and thickened epidermis and often surrounded hair follicles. Figure 4a and b shows a sagittal view. rCSLM features common to confocal images of tumors (Figure 4b and c) included melanocytic cells migrating upward into the epidermis. Figure 4c shows a series of *en face* images progressing from the surface of the skin through the epidermis into the dermis.

To the eye, the tone of the normal skin on the melanoma-induced HGF/B6 mouse was not much lighter than the tone in the melanoma lesions or the normal pigmented tissue although the confocal microscopy clearly showed an increased presence of melanotic features with strong backscattering of light in the tumors. The putative melanoma cells were large, abundant, and irregularly shaped.

In Figure 5, two axial profiles (vertical white lines, Figure 4) of reflectance are plotted versus depth, one intersecting an epidermal melanocyte and the other just adjacent. Calibration (equation 2) was applied to the data to yield reflectance units.

At the tissue surface ($z = 16 \mu\text{m}$, Figure 5) the water/stratum corneum interface reflectivity was $R_{\text{measured}} = 0.0013$. The Fresnel reflectance predicted from an interface

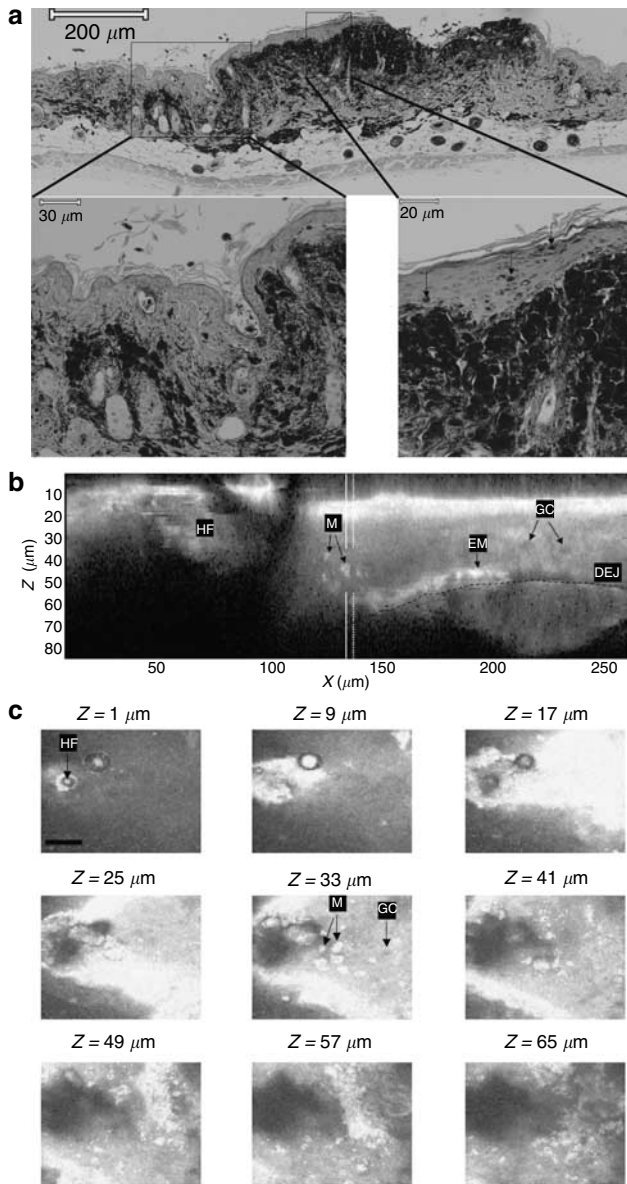


Figure 4. Melanoma. (a) Histology with an iron counter stain shows that the pigment is not iron. This late-stage tumor has ulcerated. The insets show (left) the epidermal thickening (left to right) and (right) the epidermal melanocytes indicated with arrows. In the confocal images (b, sagittal, c, *en face*) the malignant tumor is identified by bright areas of high melanin density located in single epidermal melanoma cells and at larger structures of these cells at the DEJ. HF, hair follicle (hair has been Nair'dTM) $50 \mu\text{m}$ in diameter. M, epidermal melanocytes. GC, granular cells with dark nuclei beneath the stratum corneum. Cells in the granular layer within the epidermis appear with dark nuclei, which backscatter less light than the surrounding cytoplasm/cell wall/extracellular matrix. DEJ, dermal-epidermal junction. EM, irregular groups of polymorphic melanocytes at DEJ. The white lines at $x = 132$ marks an axial z -profile that will be analyzed in Figure 5.

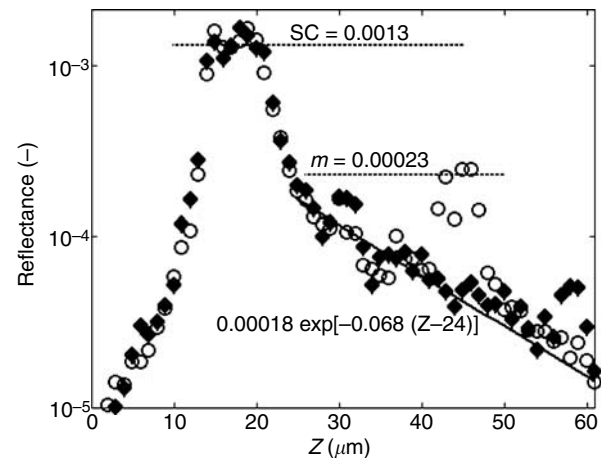


Figure 5. The axial reflectance profile through one melanocytic cell, relative to surrounding epidermis. Circles represent the data from the solid white line in Figure 4 b, diamonds represent data from the dashed white line. Centered at $z = 16 \mu\text{m}$, the reflectance of the stratum corneum (SC) is 1.3×10^{-3} . Beneath the SC, the bulk tissue reflectance decay is fit with an exponential. Centered at $z = 45 \mu\text{m}$, an epidermal melanocyte's measured peak reflectance is $m = 2.3 \times 10^{-4}$, which is 1.87×10^{-4} above the epidermal background at $z = 45 \mu\text{m}$ (4.3×10^{-5}). The decaying exponential least-squares error fit to the data, which is not sensitive to data points in the SC ($z < 24 \mu\text{m}$) or in the melanocyte ($40 > z > 48$), represents the background reflectance of the epidermis.

of water ($n_{\text{H}_2\text{O}} = 1.33$) and stratum corneum ($n = 1.51$) is $R_{\text{theoretical}} = 0.0040$. The difference between $R_{\text{theoretical}}$ and R_{measured} is probably because of roughness of the stratum corneum. At $z = 45 \mu\text{m}$, the reflectance of the melanocyte (Figure 5) was $R_{\text{mel}} = 0.00023$ and the reflectance of the background was only $R_{\text{epi}} = 0.000043$. The melanocyte stands out from the background epidermis by a factor of $R_{\text{mel}}/R_{\text{epi}} = 5.3$.

In addition to the axial decay characterization described above, an *en face* analysis was used to compare populations of tumor characteristics. Tumor cells and nests were characterized by directly comparing their reflectance to that of the laterally surrounding epidermis. Five features (melanocytic cells or tumor nests) were picked from Figure 4c along with the corresponding five adjacent normal areas. Figure 6a shows the same *en face* images as in Figure 4c replotted with the tumor features marked. A 3×3 voxel ($1.5 \times 1.5 \mu\text{m}$) square region centered on the points picked as

tumor and normal was averaged to yield the reflectance of tumor (R_t) and normal (R_n) tissue, respectively. In Figure 6a, the black open circles indicate normal sites and asterisks to indicate tumor sites. Figure 6b shows the paired points, R_t vs R_n , for the tumor and normal sites of Figure 6a. The average reflectances shown for the five pairs represent the mean and standard deviation of the nine-voxel region. Although the reflectance variability within a particular tissue was large because of the natural texture of the tissue, the mean reflectance level was consistently larger for the tumor ($R_t \approx 5.2R_n$).

Table 1 lists the mean ratio of melanocyte reflectance (R_t) to epidermal reflectance (R_n). For the five tumors imaged, the value of R_t/R_n was 5.0 ± 1.6 , which agreed with a simple model $R_t/R_n = 5.2$ (equation 1). Table 1 also includes the results from a separate tumor on the same animal and three tumors on a separate animal (images not shown).

Figure 7 compares *en face* confocal images of tumors versus normal tissue. In general, the characteristic tumor structures were strongly scattering. Two distinct forms of involvement were seen. (1) In the epidermis, atypical melanocytes and tumor nests were observed in the tumor where only normal granular cells presented in the normal. The melanocytic lesions in the mouse epidermis exhibited pagetoid spreading, characteristic of human intraepidermal melanoma cells. (2) At the basement membrane where the DEJ was flat and continuous in healthy tissue, tumors presented irregularity where the architecture of the DEJ was disrupted.

DISCUSSION

This report illustrates our attempt to image melanoma and characterize malignancy in early-stage tumors. It was a challenge to follow lesions on a living animal and prepare histology of the same region with precision. The endogenous landmarks used such as hair follicles proved insufficient to reliably and consistently correlate the confocal microscopy with the histology. Exogenous markers such as tattooing should be pursued. Comprehensive imaging for detection of

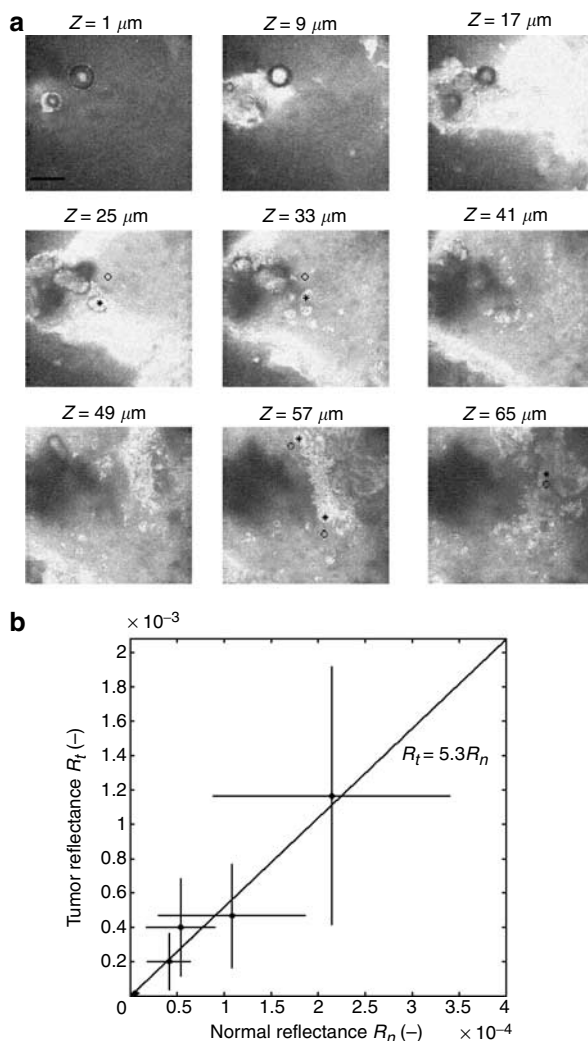


Figure 6. The contrast of melanoma. (a) Five paired tumor (*) and normal (o) sites were chosen at various depths. (b) The reflectance at the five tumor locations is shown as a function of their normal counterpart's reflectance.

Table 1. The contrast between atypical tumor features and background tissue

Tissue site	Mean R_t/R_n	SD R_t/R_n
1. Figure 5	5.0	1.6
2. Not shown	4.7	0.7
3. Not shown	6.7	1.8
4. Not shown	6.3	1.0
5. Not shown	5.3	0.7

SD, standard deviation.

The reflectance of tumor features (epidermal melanocytes or tumor cell nests) R_t is divided by the reflectance of five normal surrounding tissue R_n . Each result, the mean and SD, $n=5$ features per site for each of five tissue sites on two animals, represents the ratio R_t/R_n . The five features per site were a mixture of melanocytes and tumor nests.

epidermal tumors might include confocal mosaics (Chow *et al.*, 2006) of a large square region (~2 × 2 cm), marked by tattoo on younger animals over time with corresponding polarized light images (Jacques *et al.*, 2000, 2002; Gareau *et al.*, 2005).

This report has concentrated on illustrating two features of apparent melanoma: (1) the presence of melanocytic cells and tumor nests in the epidermis indicative of pagetoid spread and (2) disruption of the DEJ. The epidermal melanocytes and tumor nests were characterized by bright reflectance because of melanin. The relative reflectance of a melanoma cell vs background epidermis was measured to be 5.3. Five tumors additionally studied (Table 1) showed a relative reflectance of 5.6 ± 0.9. In general, the images of tumors contained a high degree of heterogeneity in rCSLM images compared with their normal counterparts.

Using these refractive indices of 1.51 for keratin, 1.7 for melanin granules, and 1.35 for background epidermis, the Fresnel reflectance (Hecht, 2002) predicted from a plane of melanin or keratin within epidermis is

$$R = ((n_{\text{epi}} - n)/(n_{\text{epi}} + n))^2 \quad (1)$$

which yields $R_{\text{ker}} = 0.0024$ and $R_{\text{mel}} = 0.014$ and the ratio $R_{\text{mel}}/R_{\text{ker}}$ is 5.8. This ratio is comparable to the fivefold ratio of melanocyte reflectance relative to that keratinocyte reflectance. The simple calculation of Fresnel reflectance from a planar interface is probably too simple to model accurately keratinocytes and melanocytes. Scattering also depends on the small particle size of keratin fibrils and melanin granules and the larger size of keratin aggregates and melanosomes. Nevertheless, the observed ratio of fivefold higher reflectivity for melanocytes relative to keratinocytes is

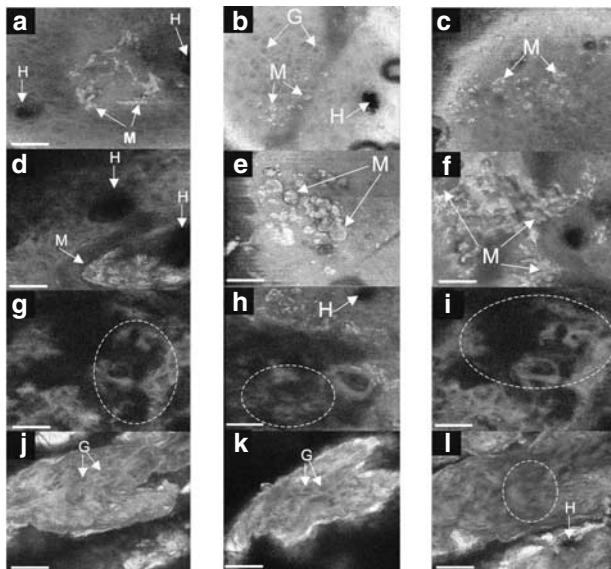


Figure 7. The characteristics of melanoma. (a–i) Tumor images versus (j–l) normal images. (a–c) Irregular epidermal melanocytes (M) in the epidermis and hair follicles (H). (d–f) A melanoma tumor nest (M) and hair follicle (H). (g–i) Disruption of the DEJ is characterized by its broken appearance. (j, k) Healthy epidermis presents granular cells with dark nuclei. (l) Approximately 10 μm below the healthy epidermis, the healthy DEJ presents as relatively uniform and intact.

consistent with the strong reflectivity expected from melanin granules. The refractive index difference of melanin granules and keratin fibrils relative to the surrounding epidermis is the expected basis of optical contrast for imaging of melanoma.

MATERIALS AND METHODS

Animals

The HGF/B6 melanoma model (Noonan *et al.*, 2001) developed at the National Cancer Institute and George Washington University was used in this study. Genetically engineered mice overexpressed HGF/scatter factor, making them susceptible to melanoma induced by UV radiation on the back (Noonan *et al.*, 2001). Mice used in this study had a pigmented C57BL/6 genetic background. The UV-irradiated HGF/B6 mouse developed melanoma through a series of stages, starting with multiple skin lesions that appeared first as small tumors (<1 mm diameter, Figure 8) followed by a progressive swelling of the dermis (Figure 2). Mice with tumors that grew to 1 cm in diameter were immediately killed and imaged, all other imaging was done *in vivo*. All animal studies were approved by the Oregon Health and Science University Institutional Animal Care and Use Committee. Hair was removed chemically (Nair™). Tumors on the lower back were imaged to avoid motion from the heart and lungs. The underside of the mice, which had not developed melanoma through UV-induced radiation was imaged as a control.

Figure 8 shows an early-stage lesion. Multiple early-stage lesions were followed through tumor development. About half of the early-stage lesions became enlarged and spread laterally. The results presented in this paper constitute a subset of the laterally spreading lesions versus normal skin.

One-year-old animals from previous collaborators’ experiments were used to minimize overall animal use. Lesions were identified by eye and then imaged with a polarized wide-field microscope (Jacques *et al.*, 2000, 2002; Gareau *et al.*, 2005) to identify lesions that were superficial and hence likely to present pagetoid melanocytes. Animals were placed on a metal plate the size and shape of a standard microscope slide, with the tumor of interest

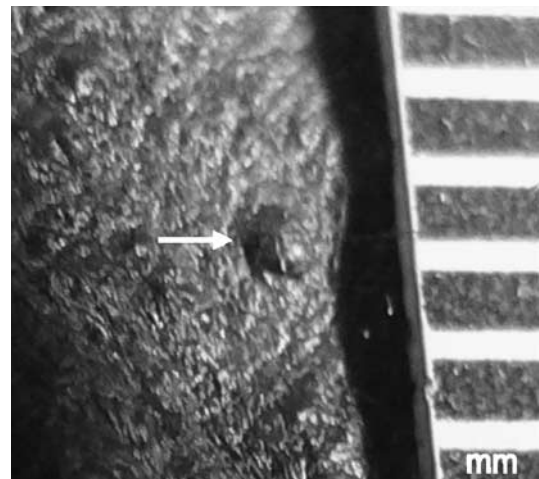


Figure 8. Digital photograph of dorsal melanoma tumor (center). Millimeter markings show the tumor’s diameter to be about 0.7 mm. The animals had already developed lesions as large as 5 mm in diameter, but also had early-stage lesions (less than 1 mm diameter), which were deemed early lesions and chosen for imaging.

centered over a 2-mm diameter hole in the plate. Optical coupling between the objective lens and the skin was achieved with a drop of saline solution. The animal was immobilized in a least invasive manner with 10 wrappings of an elastic string (Spider-Thread™, Redwing Tackle, Ontario, Canada), which is commonly used for fixing bait to fishing hooks. This sufficiently stabilized the skin to minimize movement artifacts because of heartbeat and breathing. The two-dimensional field of view (x , y , and $z=260$, 253 , and $80\ \mu\text{m}$, respectively) took about 15 minutes to acquire. The animal (36 g typical weight) was anesthetized during each 45-minute imaging session by a ketamine/xylazine cocktail (0.5 ml intraperitoneally, adjusted for animal weight, age, and tumor load).

rCSLM

An rCSLM incorporating reflectance and fluorescence channels was designed and assembled. The fluorescence mode capabilities were designed for other experiments and not used in this report. The rCSLM used a 488-nm (blue) argon ion laser, x - and y -axis scanning mirrors, original magnification $\times 60$ water-dipping objective lens (0.90 NA Olympus LUMPlanFI), a photomultiplier tube (Hamamatsu Photonics, 5773-01), a data acquisition board (National Instruments, 6062E) and a z -axis motorized stage (Applied Scientific Instrumentation, Eugene, OR, LS50A) for supporting the animal, Labview software to control the system, and a Gateway laptop computer (Microsoft Windows 2000 operating system). A relay lens system magnified the image to project the central lobe of the airy function (Rajadhyaksha and Gonzalez, 2003) to be 1.5 times larger than the $50\text{-}\mu\text{m}$ diameter pinhole for confocally matched gating (Wilson and Sheppard, 1984). The axial resolution limit measured for the system was $1.25\ \mu\text{m}$. The scanning mirrors provided x - y scans (512×512 volume elements (voxels), 25 kHz voxel acquisition rate, 10.5 seconds per image) at each depth z in the tissue. The motorized stage advanced the animal $1\ \mu\text{m}$ along the z -axis before each x - y scan 80 times ($512 \times 512 \times 80$ voxels). Post-processing of the data was carried out using MATLAB™ software.

To express voxel values in the units of optical reflectance, calibration was achieved by imaging the water/glass coverslip interface with a neutral density filter (optical density = 1.0) attenuating the laser and equating this measurement to the Fresnel reflectance for a planar water/glass interface with a refractive index mismatch $R = ((n_1 - n_2)/(n_1 + n_2))^2 = 0.0044$ for water ($n_1 = 1.33$) and glass ($n_2 = 1.52$). The reflectance (R) of the mouse skin measured without the neutral density filter was calculated based on the confocal signal in volts from the mouse (V_m) and from the water/glass interface (V_{wg}):

$$R = \frac{V_m}{V_{wg}} \frac{0.0044}{(10^{-OD})} \quad (2)$$

Typical values of R for the C57/B6 mouse skin were 10^{-5} – 10^{-4} . Voxel values in the confocal images in this report are presented as the log of the data $\log_{10}(R)$ over the range $10^{-5} < R < 10^{-3}$. This graphical display allocates the dynamic range in the image to optimally include the range of reflectance of the tissue.

Experimental protocol

The back of each animal, which had been exposed to the tumor-inducing UV radiation, was examined for tumor growth. Anesthesia

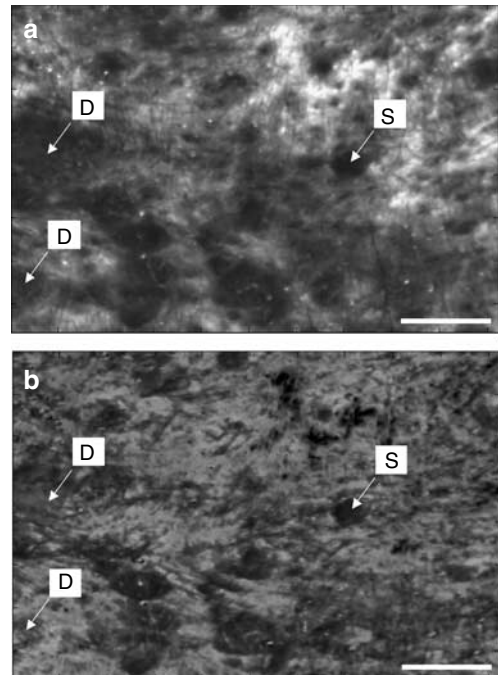


Figure 9. Polarized image of dorsal melanoma tumors. (a) Normal light image. (b) Polarized light image, based on difference between two images, one through linear polarizer oriented parallel to the polarized illumination and the second cross-polarized perpendicular to the illumination. The superficial lesion (S) appeared black in both normal-light and polarized-light images, whereas deeper lesion (D) appears black only in normal-light images. Bar = 2 mm.

was followed by digital photography (Panasonic DMC-FZ20) as shown in Figure 8, then imaging with a wide field-of-view polarized-light imaging system (Figure 9, Gareau *et al.*, 2005) that aided in finding early superficial lesions.

After selecting lesions using the polarized images, animals were immobilized on the metal plate, which was placed on the rCSLM stage. The water-dipping objective lens of original magnification $\times 60$ was coupled to the skin surface from below using phosphate-buffered saline.

Lesions were imaged one to three successive times over a 1-month period using landmarks of biological features such as tumor size, shape, and relative location as well as hair follicle location to keep track of the lesions during successive imaging sessions. At the last time point of *in vivo* imaging, the tumors were excised for histopathology with the position and orientation landmarks of the tumor noted.

CONFLICT OF INTEREST

The authors state no conflict of interest.

ACKNOWLEDGMENTS

This work was supported by the National Institutes of Health, EB000224 (SLJ), CA98893 (MKM), and CA69533 (OHSU Cancer Institute). We thank Drs. Alon Scope, Frances Noonan, Ed De Fabo, and Miriam Anver for critical review of this paper. We also thank Dr. Miriam Anver and Carolyn Gendron for histopathology.

REFERENCES

- Brunsting A, Mullaney P (1974) Differential light scattering from spherical mammalian cells. *Biophys J* 14:439–53
- Chow SK, Hakozi H, Price DL, Maclean AB, Deerinck TJ, Bouwer JC *et al.* (2006) Automated microscopy system for mosaic acquisition and processing. *J Microscopy* 222:76–84
- Gareau DS, Lagowski J, Rossi V, Viator JA, Merlino G, Kulesz-Martin M, Jacques SL (2005) Imaging melanoma in a murine model using reflectance-mode confocal scanning laser microscopy and polarized light imaging. *J Invest Dermatol Symp Proc* 10:164–9
- Greger A, Koller S, Kern T, Massone C, Steiger K, Richtig E *et al.* (2005) Diagnostic applicability of *in vivo* confocal laser scanning microscopy in melanocytic skin tumors. *J Invest Dermatol* 124:493–498
- Hecht E (2002) *Optics*. New Jersey: Pearson Education
- Jacques SL (1998) Spectrum used in online class tutorial. <http://omlc.ogi.edu/classroom/ece532/class3/muaspectra.html>
- Jacques SL, Roman J, Lee K (2000) Imaging superficial tissues with polarized light. *Lasers Surg Med* 26:119–29
- Jacques SL, Ramella-Roman JC, Lee K (2002) Imaging skin pathology with polarized light. *J Biomed Opt* 7:329–40
- Noonan FP, Recio JA, Takayama H, Duray P, Anver MR, Rush WL *et al.* (2001) Neonatal sunburn and melanoma in mice. *Nature* 413:271–2
- Rajadhyaksha M, Gonzalez S (2003) Real-time *in vivo* confocal fluorescence microscopy. In: *Handbook of biomedical fluorescence*. (Mycek MA, Pogue B, eds) New York: Marcel Dekker, 143–80
- Rajadhyaksha M, Gonzalez S, Zavislan JM, Anderson RR, Webb RH (1999) *In vivo* confocal scanning laser microscopy of human skin II: advances in instrumentation and comparison with histology. *J Invest Dermatol* 113:293–303
- Rajadhyaksha M, Grossman M, Esterowitz D, Webb RH, Anderson RR (1995) Video-rate confocal scanning laser microscopy for human skin: melanin provides strong contrast. *J Invest Dermatol* 104:946–952
- Vitkin IA, Woolsey J, Wilson BC, Anderson RR (1994) Optical and thermal characterization of natural (*sepia officinalis*) melanin. *Photochem Photobiol* 59:455–62
- Wang X, Milner TE, Chang MC, Nelson JS (1996) Group refractive index measurement of dry and hydrated type I collagen films using optical low-coherence reflectometry. *J Biomed Opt* 1:212–6
- Wilson T, Sheppard CJR (1984) *Theory and practice of scanning optical microscopy*. New York: Academic Press